Electronic states of intrinsic surface and bulk vacancies in FeS_2

2013 J. Phys.: Condens. Matter 25 045004

(http://iopscience.iop.org/0953-8984/25/4/045004)

J. Phys.: Condens. Matter **25** (2013) 045004 (11pp) doi:10.1088/0953-8984/25/4/045004

Electronic states of intrinsic surface and bulk vacancies in FeS_2

Aravind Krishnamoorthy[1,2], F. William Herbert[1,2], Sidney Yip[2,3], Krystyn J. Van Vliet[2] and Bilge Yildiz[1,3]

[1] Laboratory for Electrochemical Interfaces, Massachusetts Institute of Technology, 77 Massachusetts Avenue, Cambridge, MA 02139, USA
[2] Department of Materials Science and Engineering, Massachusetts Institute of Technology, 77 Massachusetts Avenue, Cambridge, MA 02139, USA
[3] Department of Nuclear Science and Engineering, Massachusetts Institute of Technology, 77 Massachusetts Avenue, Cambridge, MA 02139, USA

E-mail: byildiz@mit.edu

Received 23 July 2012, in final form 5 November 2012
Published 10 December 2012
Online at stacks.iop.org/JPhysCM/25/045004

Abstract
Understanding the stability and reactivity of iron sulfide phases is key to developing predictive capabilities for assessing their corrosion and catalytic activity. The differences between the free surface and the bulk interior of such phases are of particular importance in this context. Here, we employ density functional theory to investigate the formation energetics and electronic structure of intrinsic Fe and S vacancies in bulk pyrite (FeS_2) and on the pyrite (100) surface. The formation energies of intrinsic bulk vacancies of all charge states are found to be high, ranging from 1.7 to 3.7 eV. While the formation energies of surface vacancies are lower, varying from 1.4 to 2.1 eV for S vacancies and from 0.3 to 1.7 eV for Fe vacancies, they are too large to result in significant sub-stoichiometry in bulk pyrite at moderate temperatures. On the basis of charged defect formation energies and defect equilibria calculations, intrinsic charge carriers are expected to outnumber point defects by several orders of magnitude, and therefore, pure pyrite is not expected to demonstrate p-type or n-type conductivity. The presence of surface states is observed to cause a reduction in the band gap at the (100) surface, which was captured computationally and experimentally using tunneling spectroscopy measurements in this work. The vacancy-induced defect states behave as acceptor-like or donor-like defect states within the bulk band gap. The findings on the stoichiometry and the electronic structure of active sites on the (100) surface have important implications for the reactivity of pyrite.

S Online supplementary data available from stacks.iop.org/JPhysCM/25/045004/mmedia

(Some figures may appear in colour only in the online journal)

1. Introduction

Iron sulfides are a diverse group of compounds of varying stoichiometries, abundant in the Earth's crust. They are known to play an important role in the biogeochemical sulfur cycle and anoxic high-temperature corrosion processes encountered in the petrochemical industry [1]. Recently, iron disulfide, pyrite (FeS_2) has been in the spotlight for potential photovoltaic [2], battery cathode [3] and thermoelectric [4] applications. Despite this wide-ranging interest, important questions about the mechanism of pyrite oxidation and transport properties in defective pyrite (with intrinsic defects or with impurities) have not been answered fully. An aim of the present study is to contribute to the understanding of the reactivity of FeS_x phases in extreme environments that characterize corrosion processes [1, 5].

Ab initio atomistic modeling techniques, validated by suitable experiments, can advance our theoretical

understanding of these processes at the electronic and atomic level. However, well-established techniques like density functional theory (DFT) face major challenges in accurately representing the electronic and crystal structure of the different iron sulfide phases. This drawback is chiefly attributed to non-local functionals like the generalized gradient approximation (GGA), which do not reproduce the localized nature of the Fe 3d states [6]. Since GGA causes an unphysical delocalization of these electrons, it leads to significant errors in the calculated electronic properties of the material, i.e., underestimation of the band gap. This error is demonstrated in *ab initio* studies with GGA that predict that pyrite is a gap-less conductor [7], while it has been experimentally observed to have a band gap in the range of 0.85–0.95 eV using different experimental techniques such as photoconductivity [8], optical absorption [9] and x-ray absorption spectroscopy [10] measurements. Hybrid functionals such as the Becke, 3-parameter, Lee–Yang–Parr functional (B3LYP), which contain fractional non-local or Hartree–Fock exchange are good at reproducing the experimentally observed band gap in many classes of materials, but overestimate FeS_2 band gaps by as much as 100% [11]. Furthermore, hybrid functionals are computationally expensive and are not viable for performing large-scale calculations in a practical time frame. In this work, we parameterize and incorporate Hubbard U corrections to DFT (the DFT+U method), which considers on-site Coulomb interactions to model intra-atomic electronic correlations. This method has been used successfully to predict the correct electronic ground states of several transition metal oxides for which the non-hybrid DFT-GGA has failed [12, 13]. The DFT + U method has also been applied to a narrow range of 3d transition metal sulfides to reproduce their crystal and electronic structure [6, 14]. Prior work has demonstrated that a single correction parameter (i.e., a single value of U) can describe the electronic structure of a transition metal in different oxidation states [15]. This makes the DFT + U method ideally suited to model the behavior of transition metal compounds in the context of corrosion, where the oxidation state of the metal ion may change due to the environmental conditions and phase transformations.

Real sour corrosion films are multiphase systems and to be able to model reactions in such systems, methods must be developed that can best describe the physical properties of multiple iron sulfide phases, which are of relevance to corrosion, simultaneously within the same simulation cell. This capability is required to study complex processes like phase transformations and the role of phase boundaries which are important to consider in the context of corrosion. In this article we parameterize the DFT+U method, through the $U-J$ parameter, to best represent multiple iron sulfide phases. In this respect, we chose troilite (FeS), MnP-type FeS and pyrite (FeS_2) as model phases for $U - J$ parameterization because they are the most commonly encountered phases in iron sulfide corrosion systems and they are the phases with which we expect to do most of our calculations in the future. Further, we chose to use unit cell volume, bulk modulus and band gap as the properties for $U - J$ optimization as representations of the structural, mechanical and electronic properties of the phases. These properties determine important parameters, for example defect concentrations, fracture strength, ease of surface charge transfer, which govern the corrosion reactivity of surface films. While the parameterized $U - J$ value may not model any one property of any one phase with complete accuracy, our objective is to identify one that is the best compromise at representing all the three phases and all the three properties as accurately as possible. It will be seen in the results section that this approach actually enabled us to characterize the selected iron sulfide phases with very good accuracy.

Having parameterized the DFT+U model for three major FeS_x phases, we then calculate defect formation energies and identify the defect states of iron and sulfur vacancies in pyrite. This serves two purposes; (i) validation of the DFT+U model using properties that were not used in the parameterization of the DFT + U method, and (ii) to identify the impact of point defects on the electronic structure of pyrite. Pyrite was chosen for this investigation because there is abundant prior and emerging literature, both experimental and computational, on the electronic and defect structure of this phase, primarily due to interest in photovoltaic applications.

A key aim of the present study is to contribute to the understanding of iron sulfide passive films that form under anoxic, corrosive conditions where H_2S is present. The corrosion of steels in such environments is governed to a large extent by defect-mediated processes in the passive film such as surface reactions and ionic diffusion [16]. The initial growth of the passive Fe–S layer is controlled by adsorption, dissociation and diffusion of reactant (H_2S) molecules and charge transfer at the film-electrolyte interface; these unit processes have been shown to occur favorably at surface defects on pyrite [5, 17, 18]. A detailed characterization of surface electronic structure can serve as the primary input to catalytic models, such as the Fermi level DOS theory [19] or the d-band center theory [20], to qualitatively assess the reactivity of different iron sulfide phases in corrosive environments. Further corrosion of the underlying metal can be limited by bulk, vacancy-mediated diffusion in iron sulfide [21]. Finally, the breakdown or degradation of passivating Fe–S layers, for example through crack nucleation and propagation, can also be linked to intrinsic vacancies in thin films [22]. The quantification of bulk and surface defect formation energies and their associated electronic states is intended to instruct multi-scale models of Fe–S growth and degradation which are the focus of the authors' ongoing work. However, to our knowledge this correlation between point defect structure and electronic properties of pyrite has not been interrogated in detail. Here, we computationally analyze the effect of these defect states on the electronic structure of both the bulk and the surface of pyrite, and validate the predicted surface electronic structure via surface-sensitive electronic band gap measurements.

2. Methodology

2.1. Quantification of electronic correlation corrections (DFT+U method)

We adopt the DFT + U method developed by Dudarev *et al*, where the strength of the on-site Coulomb correction is given by the difference between the Coulomb (U) and exchange terms (J) [23]. Since the correction depends only on the value of $U - J$ in this scheme, the value of J was fixed to be 0 eV and optimization was done only on the U parameter. The optimization of the U parameter was performed on three FeS_x phases of relevance to anoxic corrosion, troilite, MnP-type FeS and pyrite (crystal structures are depicted in figure 1). To our knowledge, this is the first study to attempt concurrent Hubbard U parameterization for multiple iron sulfide phases[4]. This is important because the ultimate aim of the current study is to analyze and quantify the corrosion behavior of different iron sulfide phases. This entails comparison between the calculated corrosion-related properties of different iron sulfide phases. A meaningful comparison of calculated properties across different phases can be made only if DFT calculations are performed using identical simulation parameters such as energy cutoffs and $U - J$ values for all phases.

Catalytic and corrosion activity is controlled by an interplay between the material's electronic structure, transport and mechanical properties, which are represented in this study using the band gap, the unit cell volume and the bulk modulus of each phase, respectively. To optimize the U parameter, the calculated values of the three physical properties of each phase at different values of $U - J$ are compared to the experimentally determined value. The optimum value of the U parameter is one which minimizes the difference between the calculated and the experimental property values for all the phases.

2.2. Intrinsic vacancy formation energies in FeS_2

The formation energy of a defect of charge q in pyrite is given by

$$H_f = E(\text{defect} \mid q) - N_{Fe}\mu_{Fe} - N_S\mu_S + q(\varepsilon_F + \text{VBM}) \quad (1)$$

where $E(\text{defect} \mid q)$ is the energy of the supercell with the defect, N_{Fe} is the number of Fe atoms, N_S is the number of S atoms in the defective supercell, VBM is the valence band maximum, and ε_F is the Fermi level calculated from VBM. The value of VBM is calculated using the method reported by Matsunaga *et al* [24].

The dependence of defect formation energy on environmental conditions is introduced through the terms μ_S and ε_F. The first term, μ_S, quantifies the amount of sulfur in the environment, while the latter term, ε_F, encompasses the effects of internal conditions like strain state, impurity and defect concentration into a single measurable electronic structure parameter. If we assume that the pyrite crystal remains more stable relative to its constituent elements, then the chemical potentials of Fe and S in pyrite are bounded above by the chemical potential of the individual atoms in their ground state (BCC Fe and orthorhombic S, respectively). μ_{Fe} and μ^0_{Fe} (μ_S and μ^0_S) indicate the chemical potentials of iron (sulfur) in pyrite and in their native states, and the following relationships must be satisfied.

$$\mu_{Fe} < \mu^0_{Fe} = -6.83 \text{ eV/atom}$$
$$\mu_S < \mu^0_S = -4.10 \text{ eV/atom}.$$

However, the value of the chemical potentials of either element cannot be indefinitely low. Its lower limit is determined by the following relation:

$$H_f(FeS_2) = \left(\mu_{Fe} - \mu^0_{Fe}\right) + 2\left(\mu_S - \mu^0_S\right)$$
$$= -1.41 \text{ eV/formula unit} = -136.3 \text{ kJ mol}^{-1}$$

where $H_f(FeS_2)$ is the formation enthalpy of pyrite. The calculated value is less than the experimental formation enthalpy of -178 kJ mol^{-1}. This discrepancy is a well-known shortcoming of GGA functional which tend to underbind atoms. This constrains the physically valid limit for the chemical potential of sulfur in the crystal in the range:

$$\left(\tfrac{1}{2} H_f\,(FeS_2) + \mu^0_S\right) = \mu_S = \mu^0_S.$$

2.3. Computational details

All DFT calculations [25] were carried out with projector augmented wave method [26] using the Vienna Ab initio Simulation Package (VASP) [27, 28] using the Perdew–Burke–Ernzerhof (PBE) form of the GGA functional [29] with spin polarization turned on. All crystal structures in this article were generated using the VESTA visualization program [30].

The $U - J$ parameterization calculations were done with a plane wave cutoff energy of 350 eV. Total energies were converged to within 10^{-5} eV in each self-consistency cycle. The forces on ions were converged to within 0.01 eV Å^{-1}. Convergence tests were done with respect to the energy cutoff, reciprocal space k-point density (using Monkhorst–Pack grids [31]) for all calculations involving bulk phases.

Reference energies and bulk modulus were calculated on pyrite (4 formula units per supercell) with a $7 \times 7 \times 7$ k-point grid, troilite (12 formula units per supercell) with a $8 \times 8 \times 6$ k-point grid and MnP-type FeS (4 formula units per supercell) with a $11 \times 11 \times 11$ k-point grid. Reference energies and ion positions were calculated by relaxing the supercell shape, volume and ionic positions. All three phases were initialized at their magnetic ground states as reported in literature. Pyrite is non-magnetic, while troilite and MnP-type FeS are both anti-ferromagnetic with $\pm 4\mu_B$ on each Fe ion. Calculations relating to defect formation in bulk pyrite were done on $2 \times 2 \times 2$ pyrite supercells containing 32 formula units each. Reference energies of defect-free and defective crystals of pyrite were calculated by sampling the reciprocal space using a $4 \times 4 \times 4$ Monkhorst–Pack grid. Calculations of defect

[4] The suitability of the U-value found here, along with van der Waals corrections was also demonstrated on the Mackinawite phase and will be presented in a companion paper in the future by these authors.

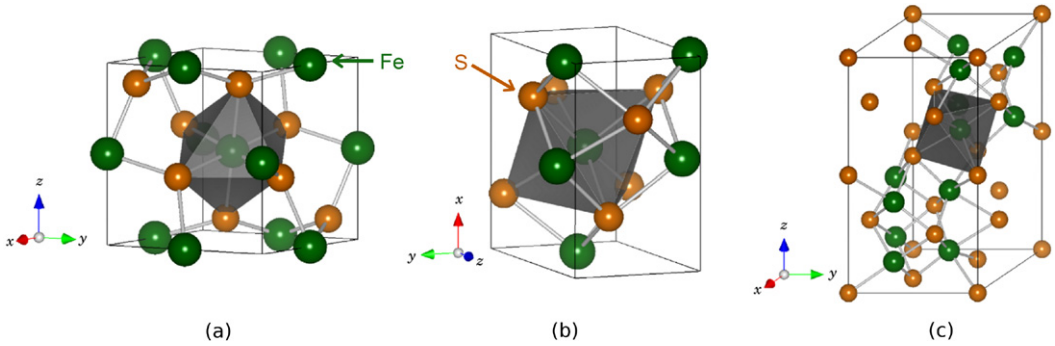

Figure 1. Iron sulfide phases, (a) pyrite (FeS_2), (b) MnP-type FeS, (c) troilite (FeS), considered for determination of DFT + U parameters along with a representative polyhedron (gray) in each structure.

formation on the pyrite (100) surface were done on $2 \times 2 \times 2$ unit cell slabs separated by 10 Å of vacuum. The thickness of the slab and the amount of vacuum was chosen such that the surface energy of the (100) surface was converged to within 0.03 J m^{-2}. Further, comparison to calculations on $2 \times 2 \times 5$ unit cell slab indicate that surface vacancy formation energies are also converged to within 0.01 eV per defect for both Fe and S vacancies. In all slab calculations, the top 2 surface S–Fe–S layers are allowed to relax while the other layers are fixed at their bulk positions. The reciprocal space was sampled with a $4 \times 4 \times 1$ Monkhorst–Pack grid. Total energy and ion-force convergence criteria for both types of calculations remain same as described previously.

2.4. Experimental details

Single crystal pyrite samples were made by chemical vapor transport in the presence of Br as a transport agent. Powders were obtained from Alfa Aesar (Haverhill, Massachusetts). Fe powder of 99.999% purity was mixed with 99.995% pure S powder in a 1:2 stoichiometric ratio and sealed under vacuum in a 20 long cm quartz tube with about 0.2 g of 98% anhydrous $FeBr_3$. The elements were pre-reacted at 600 °C for two days until they formed polycrystalline pyrite aggregates, removed and re-sealed in another similar quartz tube. The polycrystalline pyrite was subsequently placed at the hot end of a temperature gradient from 700 to 550 °C in a two-zone furnace and left for >10 days. The resulting single crystals were either cuboidal or octahedral in shape with linear dimensions on the order of 5 mm, comparable to crystals synthesized by other authors using a similar technique [32, 33]. Growth faces were identified to be either (100) or (111) by electron back-scattered diffraction (EBSD) in a Zeiss Supra-55 scanning electron microscope. The phase purity and the bulk band gap of the crystals were confirmed with Raman spectroscopy and photo-absorption measurements (figure S2 available at stacks.iop.org/JPhysCM/25/045004/mmedia).

For identifying the surface electronic structure, scanning tunneling spectroscopy (STS) was performed using an Omicron VT-AFM system (Omicron Nanotechnology, GmbH, Germany) under ultra high vacuum (UHV). Immediately prior to STS, the sample was degreased in acetone and cleaned in methanol. No further *in situ* cleaning procedures were used in addition to this. Under a stable imaging current, point tunneling spectra were obtained at various locations on the sample growth face by temporarily removing the feedback current and ramping the Pt/Ir tip bias between −2.5 and 2.5 V.

3. Results and discussion

3.1. Identification of the optimal $U - J$ value

To identify the optimum U parameter, the physical properties discussed above (section 2.1) were calculated for U values from 0 eV (pure GGA) to $U = 3.5$ eV in steps of 0.25 eV. As figure 2 demonstrates, this variation of U results in a dramatic change in certain properties as the troilite pyrite band gap, while other properties as the pyrite cell volume and MnP-type FeS band gap remain almost unchanged. This is consistent with the fact that non-hybrid and uncorrected DFT calculations on pyrite have shown good agreement with experiments for structural parameters, but not for electronic parameters [7]. Because the MnP-type FeS band gap (that is 0 eV) is insensitive to the $U - J$ values explored, we disregard this property during our calculation of the optimum $U - J$ parameter. The calculation of bulk elastic modulus for MnP-type FeS is particularly problematic for *ab initio* methods, and the two previous attempts to calculate the bulk modulus using DFT resulted in values of 76.8 GPa [34] and 73.1 GPa [35], both very different from the experimentally determined values of 44 GPa [36] and 35 GPa [37]. We suspect that temperature-dependent magnetic spin transitions [38], which are not reproduced with DFT calculations at 0 K contribute to discrepancies between experiments and DFT calculations on this property. Additionally, Ono *et al* [35] suggested that the experimental value may be in error due to the particular difficulty in calculating the bulk modulus of a phase with a very narrow stability field (3 to 7 GPa).

The troilite crystal structure is not stable at $U - J$ values exceeding 2 eV. At higher values, the crystal structure reverts back into the more symmetric NiAs crystal structure on which the troilite crystal structure is based. While it is possible to constrain the crystal to remain in the troilite crystal structure, such calculations will not be compatible with calculations done on other phases. Therefore, data points for $U > 2$ eV

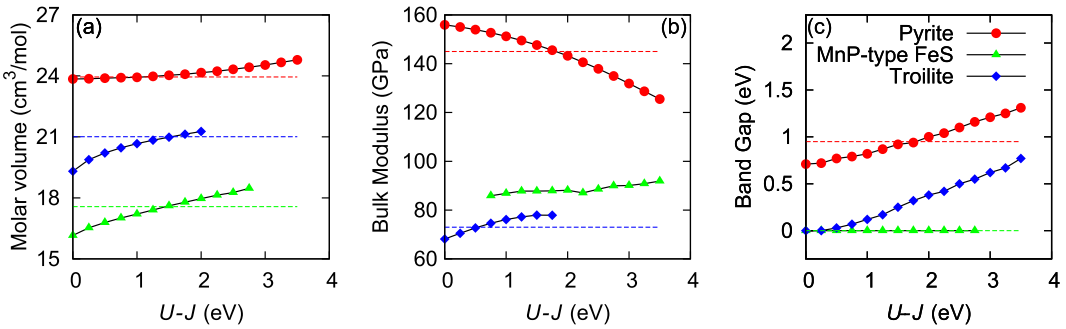

Figure 2. Variation of (a) molar volume, (b) bulk modulus and (c) bulk band gap of FeS_x phases as a function of the $U - J$ value. Dashed lines indicate the experimentally determined values for each parameter in the corresponding phase. In (c), the experimental band gaps for the troilite and MnP-type FeS phases are represented by a single dashed line at 0 eV.

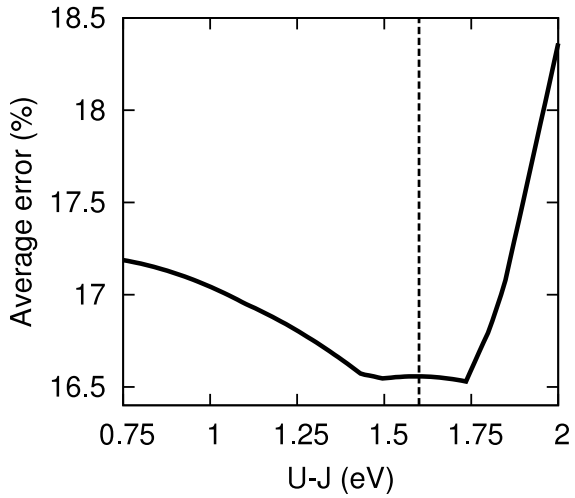

Figure 3. Optimal value of $U - J$ that minimizes total errors for all the properties of the three FeS_x phases. Note that most of the average error stems from error in the bulk modulus of MnP-type FeS (12.5%) as discussed in the text. The average error in the remaining properties is less than 4% for $U - J = 1.6$ eV.

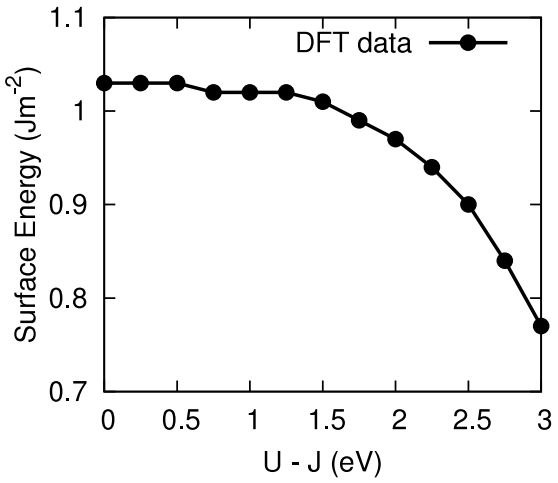

Figure 4. Variation of pyrite (100) surface energy with the $U - J$ value. At the optimal value of $U - J = 1.6$ eV, the pyrite (100) surface energy is 1.00 Jm^{-2}.

are excluded from figure 2. Experimentally, it is known that the compressibility of troilite increases with pressure [37]. Therefore, its bulk modulus increases with increasing unit cell volume or equivalently, the $U-J$ parameter. This trend is only followed in the region $U - J \leq 2$ eV for which data points are presented.

The errors in the calculated properties (as a percentage of the experimentally determined value) were weighted equally and summed up, and the optimum U parameter is chosen as the one that yields the minimum average error. The net total of errors from these properties for all three phases is minimized when $U - J = 1.6$ eV (figure 3). This is the Hubbard correlation correction that best describes the FeS_x phases considered here. The average error at $U - J = 1.6$ eV is comprised chiefly of error in the bulk modulus of MnP-type FeS (12.5% out of 16.5%). The average error in the remaining properties is less than 4%. This value for the $U - J$ parameter for FeS_x phases also agrees with previously determined values for $Fe_xMn_{1-x}S_2$ ($U = 3$ eV, $J = 1$ eV) [39] and troilite and NiAs-type FeS phases ($U - J = 1$ eV) [6].

3.2. Surface energy of pyrite (100)

To our knowledge, there are no experimentally reported values for the surface energy of the pyrite (100) face. As figure 4 shows, the calculated surface energy of pyrite (100) remains unchanged at around 1.03 Jm^{-2} for all $U-J$ values between 0 and 1.5 eV. The surface energy drops noticeably for further increases in the $U - J$ parameter. At the optimal value of $U - J = 1.6$ eV, the pyrite (100) surface energy is 1.00 Jm^{-2}, which compares well with previously reported theoretical values of 1.04 and 1.06 Jm^{-2} [14, 40]. While both prior studies used the PBE functional, only the former has made use of the DFT + U correction with a $U - J$ value of 2 eV.

3.3. Neutral and charged defects in bulk pyrite

The intrinsic point defects that were investigated in this study include both Fe and S vacancies of different charge states, including neutral, singly charged and doubly charged states. In the Kröger–Vink notation, they are denoted as $V_{Fe}^{\times}$, V'_{Fe}, V''_{Fe} and $V_S^{\times}$, $V_S^{\bullet}$ and $V_S^{\bullet\bullet}$, respectively, for Fe and S. Previous studies indicate relatively higher formation energies

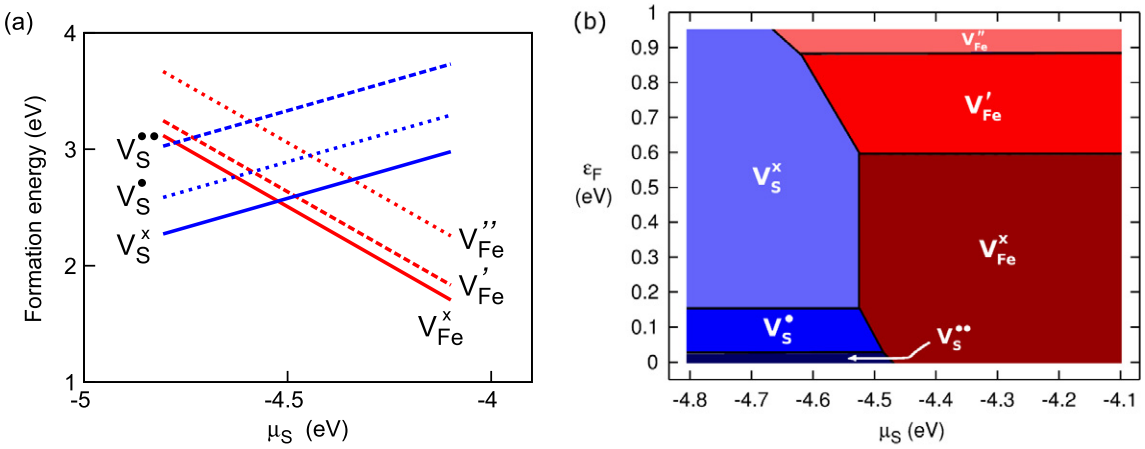

Figure 5. (a) Formation energies of differently charged Fe and S vacancies as a function of μ_s at $\varepsilon_F = 0.46$ eV. (In our calculations, the Fermi level ε_F was found constant at 0.46 eV above the VBM for all allowed values of μ_S.) (b) Predominance map depicting the regions in the $\mu_S - \varepsilon_F$ space where the different types of vacancies have the least formation energy, and thus, the highest dominance.

Table 1. Vacancy formation energies in pyrite. Where possible, defect formation energies are shown from high μ_S to low μ_S within the allowed range.

	Fe vacancy (neutral) (eV)	Sulfur vacancy (neutral) (eV)	Schottky defect (eV)
This study	1.70–3.12	2.97–2.27	7.66 (non-interacting) 5.07 (interacting)
Reference [43] (analytical)	2.54	2.32	7.18
Reference [44] (analytical)	2.18	1.66	5.50
Reference [41] (DFT calculations)	1.8–3.3	3.5–2.7	8.7

for intrinsic interstitial defects in pyrite [41], and hence they were not included in the present study.

As shown in figure 5(a), the formation energies of intrinsic vacancies are too large to induce a large off-stoichiometry at equilibrium, as also indicated computationally in [41, 42]. Charge carriers in a semiconductor can be produced either in pairs by excitation of electrons across the band gap, or singly as a co-product during the formation of a charged vacancy. In pyrite, the formation energies of charged vacancies are larger than 1.7 eV (figure 5(a)), while the band gap is only 0.95 eV. Therefore, the number of charge carriers (electrons or holes) created during the formation of charged vacancies is expected to be much smaller than the number of charge carriers created by excitation across the smaller band gap. Hence, a pure pyrite crystal (with no extrinsic defects) is expected to be an intrinsic conductor and does not display any p-type or n-type conductivity. Among the intrinsic vacancies, the neutral vacancies $V_{Fe}^{\times}$ and $V_S^{\times}$ are the most stable defects for much of the $\varepsilon_F - \mu_S$ space in bulk pyrite (figure 5(b)). This is not the case with point defects in materials with a much larger band gap than that of FeS_2, such as Al_2O_3 ($E_g =$ 8.7 eV), for which the highest possible charge state for the given vacancy is the most stable charge state for a wide range of ε_F [24].

Note that the Fermi level, ε_F, is not an independent variable. Instead, the value of the Fermi level adjusts itself to ensure that the defective crystal is charge neutral. Using the formation energies reported for the entire range of μ_S and ε_F for pyrite here, the relative concentration of the different vacancies was calculated while maintaining self-consistency

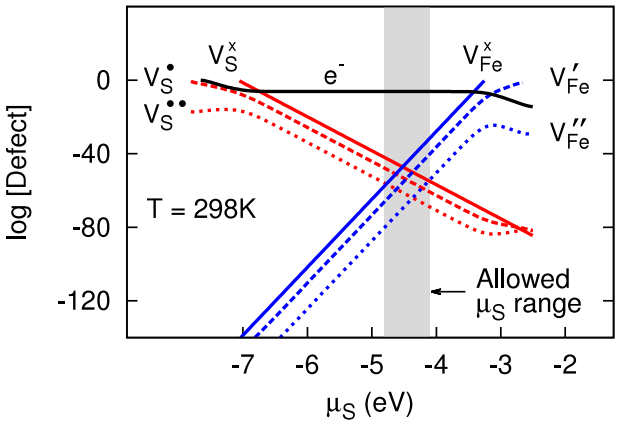

Figure 6. Concentration of S and Fe vacancies and electronic charge carriers in pyrite. In the allowed range of sulfur chemical potential, μ_S, pyrite is an intrinsic conductor.

of the Fermi level, after Sun *et al* [41], to obtain the Brouwer diagram shown in figure 6. In our calculations, the Fermi level ε_F was found constant at 0.46 eV above the VBM for all allowed values of μ_S.

Despite the large formation energies, neutral vacancies are the most abundant point defects of any charge state. Therefore we use these neutral vacancy formation energies to calculate the Schottky defect formation energies. The Schottky defect formation energy compares well with experimental–analytical models which were used to calculate the vacancy formation energy, as shown in table 1.

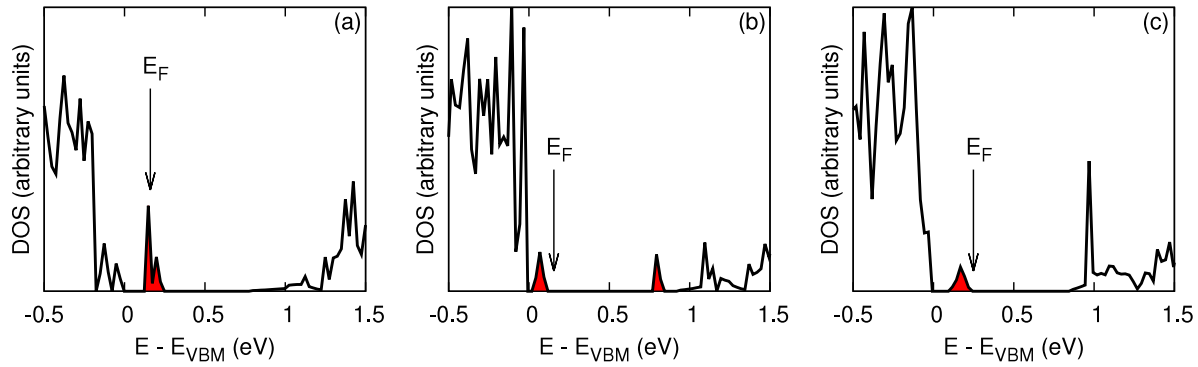

Figure 7. Position of neutral defect states (red) in the total density of states (DOS) plots of bulk pyrite due to (a) Fe vacancy, (b) S vacancy and (c) S_2 dimer vacancy.

We also note that the Schottky defect formation energy of 7.66 eV corresponds to the creation of 2 S vacancies and 1 Fe vacancy, none of which interact with each other. The energy penalty for the formation of a cluster of three neighboring and interacting Fe and S vacancies is found to be lower at 5.07 eV per Schottky defect cluster. This value is more in line with the value predicted by [44], while the non-interacting Schottky defect formation energy is more consistent with the value predicted by [43]. To calculate the vacancy formation energies, Fiechter [43] has used the macroscopic cavity method proposed by Van Vechten [45]. Ellmer *et al* [44] also have used the general principle outlined by Van Vechten, but have improved the empirical inputs to the macroscopic cavity model to obtain a Schottky defect formation energy of 5.5 eV. These values vary significantly from the value of 0.3 eV per Schottky defect reported by Birkholz *et al* [46]. The large Schottky defect formation energies reported in this work as well as in [43, 44], along with the large formation energies for each defect, explain the very small sulfur sub-stoichiometry observed in synthetically prepared pyrite samples [44].

3.4. Electronic structure of point defects in bulk pyrite

The electronic properties of pyrite may be strongly influenced by the presence of native defects via a self-doping effect even if present at ppm-concentrations. The location of the defect states due to both the Fe and S neutral vacancies is shown in figure 7. The defect levels produced by the Fe vacancy in the electronic structure are acceptor-like states in the band gap, created due to the breakage of the Fe–S bond in pyrite. In contrast, a sulfur vacancy creates two distinct defect levels in the band gap. These defect states result from the breakage of two distinct types of bonds: the Fe–S bond, and the S-S dimer bond. If enough of either defect is created, they can cause a change in the position of the Fermi level from near the center of the band gap towards one of the band edges. The Fermi level can also be changed due to the presence of charged defects, some of whose density of states (DOS) does not differ significantly from that of neutral defects except for the location of the Fermi level (see figure 8). This variation of the Fermi level (i.e., state occupancy) can be used as a basis to understand the reactivity of the pyrite crystal using well-established theoretical models like the d-band center theory [20].

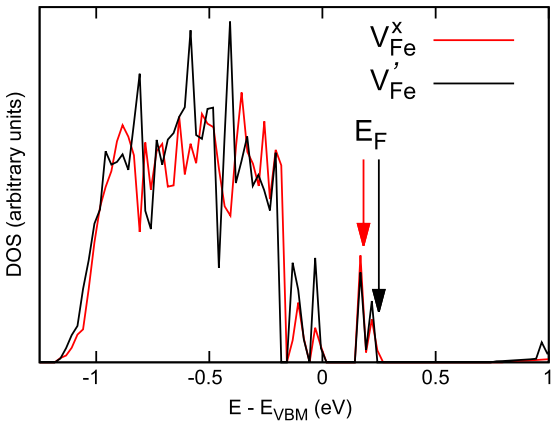

Figure 8. Charge state of a given defect changes the Fermi level of the system, but not the total density of states (DOS)—shown here for the neutral and singly charged Fe vacancies.

3.5. Electronic structure of the pyrite (100) surface

Because the pyrite (100) is the surface with the lowest surface energy and is therefore the surface most frequently formed during crystal growth or cleavage, it has been the subject of prior studies related to catalysis [5, 47, 48]. As has been found in previous studies [49], the atoms on the (100) surface do not relax appreciably from their bulk-terminated positions. The electronic structure of the (100) surface is expected to be noticeably different from that of bulk pyrite. Experimental reports that probe the surface band gap on pyrite are scarce, however, they indicate a smaller band gap than 0.95 eV observed in the bulk [50, 51]. Previous first-principles calculations with DFT-GGA without a U-correction have shown a surface band gap of 0.16 eV (the corresponding bulk band gap was calculated to be 0.65 eV) [49] and 0.4 eV (versus 0.87 eV in the bulk) [52]. Recent DFT + U calculations with $U = 2$ eV have shown that the direct band gap of the high-spin (100)

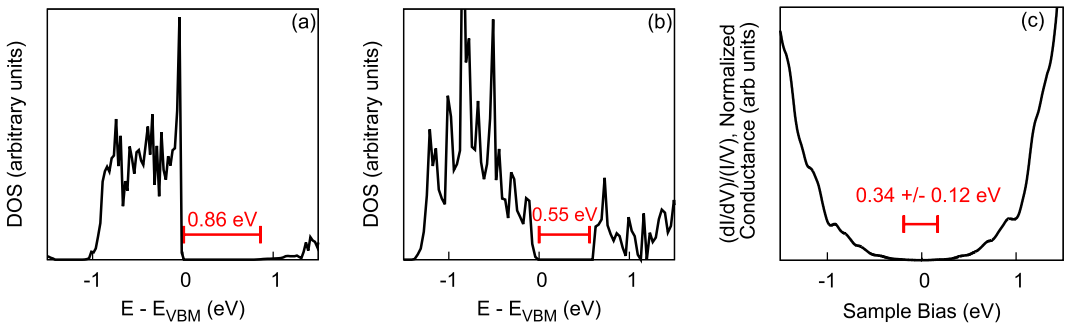

Figure 9. Calculated (a), (b) and experimental (c) electronic structure (DOS) of the defect-free pyrite bulk (a) and surface (b), (c). Both the experiments and calculations show a reduction of the surface band gap compared to the pyrite bulk.

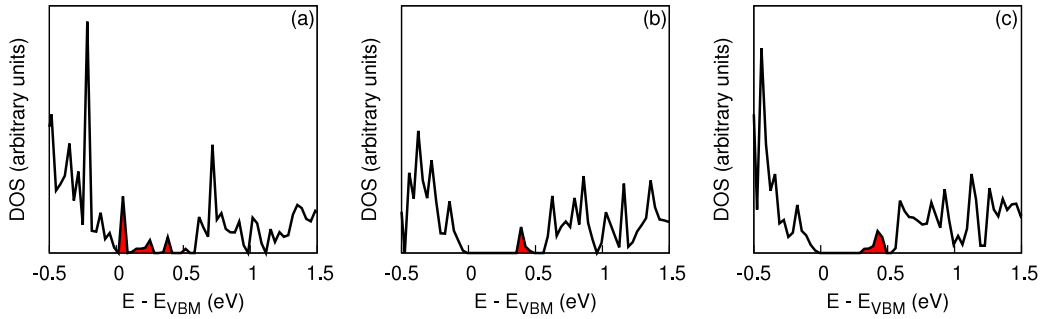

Figure 10. Position of neutral defect states (red) in the total density of states plots of the pyrite (100) surface due to (a) Fe vacancy, (b) *S* vacancy and (c) S_2 dimer vacancy.

surface is 0.72 eV [53]. We also observe such a band gap reduction at the surface using the Hubbard *U*-corrected DFT model. Using our model, the band gap observed at the surface is 0.55 eV, smaller than our computationally obtained bulk band gap of 0.86 eV. We have validated this theoretically obtained reduction in the band gap on the surface by conducting tunneling spectroscopy measurements on the (100) surface of a synthetically grown sample of pyrite as described in section 2.4. Our experimentally measured band gap on the surface is 0.34 ± 0.12 eV, as shown on the tunneling spectroscopy plot in figure 9. Both our computational and experimental results consistently demonstrate a significant reduction of the band gap on the (100) surface compared to the pyrite bulk. On the other hand, there are quantitative differences between the measured and computed values of the surface band gap (0.34 eV versus 0.55 eV, respectively). One possible explanation for this discrepancy may be the fact that it is very challenging to obtain adsorbate- and defect-free pristine pyrite surfaces in experiments. Indeed, for the surface band gap estimate, we modeled the perfect pyrite surfaces without any adsorbed atoms or surface vacancies. As we show from our DFT calculations below, the presence of defects introduces defect states in the surface band gap, and this would lead to an apparent reduction in the observed band gap in the tunneling spectroscopy measurements. Alternatively, the pyrite (100) surface has also been shown to have unit cell-high steps on the surface [51]. These surface steps can lead to a lower surface band gap due to the introduction of defect states at the step edges. Computational uncertainties also contribute to the differences between the experimental and theoretically obtained surface band gap. The *U* parameter used in calculating the surface band gap was benchmarked only using the bulk properties and did not take into account the surface terminations. We wish only to highlight the substantial reduction in the band gap at the surface (versus the bulk band gap) and the experimental work is presented to demonstrate that such a reduction is realistic and of the right order. According to the ligand field model developed by Bronold *et al* [54], the reduction in the band gap is due to formation of surface states within the bulk band gap that are a result of disturbing the octahedral symmetry around the Fe atom in bulk pyrite. While their model predicts the existence of two discrete surface states inside the bulk band gap, the surface states in the present study are found at the edges of (and remain part of) the valence and the conduction band for all investigated values of the *U* parameter (figure S1 available at stacks.iop.org/JPhysCM/25/045004/mmedia). This observation of a surface DOS with no discrete surface states (figure 9(b)) inside the band gap is consistent with previous *ab initio* studies on the (100) surface [14]. This band gap reduction is of interest to corrosion and catalysis studies chiefly because the smaller band gap can aid in electron excitation to the conduction band and its subsequent transfer to an adsorbed reactant on the surface.

3.6. Neutral defects on the pyrite (100) surface

The predominance of neutral charge state defects in bulk pyrite provides a motivation for investigating neutral defects

Table 2. Formation energy of neutral Fe and S vacancies on the pyrite (100) surface.

Fe vacancy (neutral)	S vacancy (neutral)	Schottky defect
0.26–1.67 eV	2.13–1.42 eV	4.51 eV

on the (100) surface. Another reason for limiting the study to neutral defects is the desire to avoid less accurate DFT calculations involving systems with charged surfaces. The formation energies of both the neutral Fe and S vacancies on the (100) surface are considerably less than in bulk pyrite, as shown in table 2. The lower vacancy formation energy at the surface indicates that the concentration of defects and the corresponding off-stoichiometry at the surface are expected to be higher than in the bulk. However, even these reduced defect formation energies cannot account for the large sulfur sub-stoichiometries observed in previous work [55]. We note that the vacancy formation energies found on pyrite (100) in this work are considerably higher than those reported recently by Zhang *et al* [53]. We think the discrepancy arises because of the different initial spin states of pyrite (100) slab in the two studies. Our relaxed (100) surface is low-spin, in agreement with experiments that report non-magnetism in pyrite nanocrystals [9], and contrary to the net magnetic moment of 4 μ_B on surface Fe ions in [53]. While the exact value of the sulfur vacancy formation energy needs to be determined with specific surface-sensitive experiments (which is part of our ongoing work), results from both our and Zhang *et al*'s work indicate the relatively easier formation of sulfur vacancies on the pyrite surface. The relatively lower formation energy of Fe vacancies (compared to that of S vacancies) on the surface has been previously reconciled with often-reported sulfur deficiency by demonstrating that most of the experimental observations were conducted on samples prepared in environments that were iron-rich [41]. In our calculations, we found that, in the upper limit of μ_{Fe}, the formation energy of a Fe vacancy was 1.67 eV, which is slightly higher than the calculated formation energy of a S vacancy (1.42 eV) under the same conditions. This difference in formation energies may explain, in part, the often observed S-deficiency rather than Fe-deficiency. Alternatively, naturally observed sulfur deficiency in pyrite may be due to the presence of small amounts of sulfur deficient iron sulfide phases such as pyrrhotites [56]. Substitutional defects, such as oxygen, on sulfur sites in pyrite have previously been shown to have smaller formation energies than native sulfur vacancies [41]. If such substitutional defects have sufficiently low formation free energies under driving chemical potential conditions, they may also contribute to an apparent sulfur deficiency.

The vacancy-induced defect states on the (100) surface of pyrite, shown in figure 10, are similar to those observed in the bulk. However, the twin-defect-state structure observed in figure 7(b) due to the sulfur mono-vacancies in the bulk is replaced by a single defect state on the surface. The single defect state that was observed for a Fe vacancy in bulk FeS_2 splits and broadens into multiple states in the surface band gap and results in the formation of a pseudo-metallic surface. This is because the Fe atom 'exposed at the surface' is actually located lower than a layer of surface S atoms and the removal of such a subsurface Fe atom results in large relaxations of the neighboring atoms. The root-mean-squared displacement of atoms during such a relaxation is nearly three times as much as the displacements due to removal of a surface S atom. These large relaxations result in a less localized defect state for the Fe vacancy compared to that for the S vacancy.

4. Summary

Experimental data from three iron sulfide phases—pyrite, troilite and MnP-type FeS—was used to optimize the Hubbard U parameter such that the DFT + U model simultaneously describes all three phases accurately. We used this model to calculate the formation energies and concentrations of intrinsic charged vacancies in the bulk and surface of pyrite, and their effect on the crystal's electronic structure. The formation energy for all bulk vacancies was found to be too high to induce any off-stoichiometry in bulk pyrite, and the concentration of intrinsic charge carriers was estimated to be several orders of magnitude greater than the concentration of bulk charged and uncharged vacancies. While the calculated vacancy formation energies at the (100) surface are lower than those in the bulk, no significant deviation from the ideal stoichiometry is predicted at ambient temperatures. Intrinsic bulk vacancies induce the formation of defect states in the band gap, where anion vacancies form donor-like defect states while cation vacancy states are more acceptor-like. A reduction in symmetry at the (100) surface caused the formation of surface states connected to the edges of the valence and conduction bands. The presence of these surface states is responsible for the marked reduction in the band gap of the pyrite from 0.86 eV in the bulk to 0.55 eV on the (100) surface. The reduction of the surface band gap is validated by our tunneling spectroscopy measurements on a synthetic pyrite single crystal. The reduction of the band gap at the pyrite surface and the presence of defect states in the gap have important implications for electronic processes such as charge transfer reactions at the surface as in catalysis and corrosion. An extended study on the influence of defect states on such reactions is currently being pursued by the authors as part of an ongoing study of iron sulfide corrosion films.

Acknowledgments

We gratefully acknowledge support provided by BP PLC through the BP-MIT Center for Materials and Corrosion Research and by the National Science Foundation for the computational resources provided through the Texas Advanced Computing Center under Grants No. TG-DMR110004 and No. TG-DMR120025. We thank G Ceder and R Sun for helpful review and discussions on this work. AK thanks D Marrocchelli for discussions and technical support.

References

[1] Rickard D and Luther G W 2007 Chemistry of iron sulfides *Chem. Rev.* **107** 514–62

[2] Ennaoui A *et al* 1993 Iron disulfide for solar energy conversion *Sol. Energy Mater. Sol. Cells* **29** 289–370

[3] Strauss E, Golodnitsky D and Peled E 2000 Study of phase changes during 500 full cycles of Li/composite polymer electrolyte/FeS_2 battery *Electrochim. Acta* **45** 1519–25

[4] Kato K *et al* 1997 The thermoelectric properties of FeS_2 *J. Mater. Sci. Lett.* **16** 914–6

[5] Murphy R and Strongin D R 2009 Surface reactivity of pyrite and related sulfides *Surf. Sci. Rep.* **64** 1–45

[6] Rohrbach A, Hafner J and Kresse G 2003 Electronic correlation effects in transition-metal sulfides *J. Phys.: Condens. Matter* **15** 979–96

[7] Muscat J *et al* 2002 First-principles studies of the structural and electronic properties of pyrite FeS_2 *Phys. Rev.* B **65** 054107

[8] Ho C H, Y S Huang and Tiong K K 2006 Characterization of near band-edge properties of synthetic *p*-FeS_2 iron pyrite from electrical and photoconductivity measurements *J. Alloys Compounds* **422** 321–7

[9] Bi Y *et al* 2011 Air stable, photosensitive, phase pure iron pyrite nanocrystal thin films for photovoltaic application *Nano Lett.* **11** 4953–7

[10] Wadia C *et al* 2009 Surfactant-assisted hydrothermal synthesis of single phase pyrite FeS_2 nanocrystals *Chem. Mater.* **21** 2568–70

[11] Muscat J, Wander A and Harrison N M 2001 On the prediction of band gaps from hybrid functional theory *Chem. Phys. Lett.* **342** 397–401

[12] Anisimov V I, Kuiper P and Nordgren J 1994 First-principles calculation of NiO valence spectra in the impurity-Anderson-model approximation. *Phys. Rev.* B **50** 8257

[13] Nekrasov I A *et al* 2003 Influence of rare-earth ion radii on the low-spin to intermediate-spin state transition in lanthanide cobaltite perovskites: $LaCoO_3$ versus $HoCoO_3$ *Phys. Rev.* B **68** 235113

[14] Sun R, Chan M K Y and Ceder G 2011 First-principles electronic structure and relative stability of pyrite and marcasite: implications for photovoltaic performance *Phys. Rev.* B **83** 235311

[15] Wang L, Maxisch T and Ceder G 2006 Oxidation energies of transition metal oxides within the GGA+*U* framework *Phys. Rev.* B **73** 195107

[16] Macdonald D D 1999 Passivity—the key to our metals-based civilization *Pure Appl. Chem.* **71** 951–78

[17] Guevremont J M, Strongin D R and Schoonen M A A 1998 Thermal chemistry of H_2S and H_2O on the (100) plane of pyrite: unique reactivity of defect sites *Am. Mineral.* **83** 1246–55

[18] Wahlström E *et al* 2004 Electron transfer-induced dynamics of oxygen molecules on the TiO_2(110) surface *Science* **303** 511–3

[19] Feibelman P J and Hamann D R 1984 Electronic structure of a 'poisoned' transition-metal surface *Phys. Rev. Lett.* **52** 61–4

[20] Hammer B and Nørskov J K 1995 Electronic factors determining the reactivity of metal surfaces *Surface Sci.* **343** 211–20

[21] Hernández-Espejel A *et al* 2010 Investigations of corrosion films formed on API-X52 pipeline steel in acid sour media *Corros. Sci.* **52** 2258–67

[22] Galvele J R 1993 Surface mobility mechanism of stress-corrosion cracking *Corros. Sci.* **35** 419–34

[23] Dudarev S L *et al* 1998 Electron-energy-loss spectra and the structural stability of nickel oxide: an LSDA+*U* study *Phys. Rev.* B **57** 1505

[24] Matsunaga K *et al* 2003 First-principles calculations of intrinsic defects in Al_2O_3 *Phys. Rev.* B **68** 085110

[25] Kohn W and Sham L J 1965 Self-consistent equations including exchange and correlation effects *Phys. Rev.* **140** A1133

[26] Blöchl P E 1994 Projector augmented-wave method *Phys. Rev.* B **50** 17953

[27] Kresse G and Furthmüller J 1996 Efficiency of *ab initio* total energy calculations for metals and semiconductors using a plane-wave basis set *Comput. Mater. Sci.* **6** 15–50

[28] Kresse G and Furthmüller J 1996 Efficient iterative schemes for *ab initio* total-energy calculations using a plane-wave basis set *Phys. Rev.* B **54** 11169

[29] Perdew J P, Burke K and Ernzerhof M 1996 Generalized gradient approximation made simple *Phys. Rev. Lett.* **77** 3865

[30] Momma K and Izumi F 2008 VESTA: a three-dimensional visualization system for electronic and structural analysis *J. Appl. Crystallogr.* **41** 653–8

[31] Monkhorst H J and Pack J D 1976 Special points for Brillouin-zone integrations *Phys. Rev.* B **13** 5188

[32] Bronold M, Pettenkofer C and Jaegermann W 1994 Surface photovoltage measurements on pyrite(100) cleavage planes—evidence for electronic bulk defects *J. Appl. Phys.* **76** 5800–8

[33] Lehner S and Savage K 2008 The effect of As, Co, and Ni impurities on pyrite oxidation kinetics: batch and flow-through reactor experiments with synthetic pyrite *Geochim. Cosmochim. Acta* **72** 1788–800

[34] Martin P, Price G D and Vocadlo L 2001 An *ab initio* study of the relative stabilities and equations of state of FeS polymorphs *Mineral Mag.* **65** 181–91

[35] Ono S *et al* 2008 High-pressure phase transformations of FeS: Novel phases at conditions of planetary cores *Earth Planet. Sci. Lett.* **272** 481–7

[36] Kusaba K *et al* 1997 Structure of FeS under high pressure *J. Phys. Chem. Solids* **58** 241–6

[37] King H E Jr and Prewitt C T 1982 High-pressure and high-temperature polymorphism of iron sulfide (FeS) *Acta Crystallogr.* B **38** 1877–87

[38] Kruse O 1993 Spin flip and troilite-MnP structure transition in FeS as studied by Mössbauer spectroscopy *J. Phys. Chem. Solids* **54** 1593–7

[39] Persson K, Ceder G and Morgan D 2006 Spin transitions in the $Fe_xMn_{1-x}S_2$ system *Phys. Rev.* B **73** 115201

[40] Hung A *et al* 2002 Density-functional theory studies of pyrite FeS_2(100) and (110) surfaces *Surf. Sci.* **513** 511–24

[41] Sun R *et al* 2011 Intrinsic stoichiometry and oxygen-induced *p*-type conductivity of pyrite FeS_2 *Phys. Rev.* B **84** 035212

[42] Hu J *et al* 2012 First-principles studies of the electronic properties of native and substitutional anionic defects in bulk iron pyrite *Phys. Rev.* B **85** 085203

[43] Fiechter S 2004 Defect formation energies and homogeneity ranges of rock salt-, pyrite-, chalcopyrite- and molybdenite-type compound semiconductors *Sol. Energy Mater. Sol. Cells* **83** 459–77

[44] Ellmer K and Höpfner C 1997 On the stoichiometry of the semiconductor pyrite (FeS_2) *Phil. Mag.* A **75** 1129–51

[45] Van Vechten J A 1975 Simple theoretical estimates of the Schottky constants and virtual-enthalpies of single vacancy formation in zinc-blende and wurtzite type semiconductors *J. Electrochem. Soc.* **122** 419–22

[46] Birkholz M *et al* 1991 Sulfur deficiency in iron pyrite (FeS_{2-x}) and its consequences for band-structure models *Phys. Rev.* B **43** 11926

[47] Guevremont J M *et al* 1998 Structure sensitivity of pyrite oxidation: comparison of the (100) and (111) planes *Am. Mineral.* **83** 1353–6

[48] Sacchi M, Galbraith M C E and Jenkins S J 2012 The interaction of iron pyrite with oxygen, nitrogen and nitrogen oxides: a first-principles study *Phys. Chem. Chem. Phys.* **14** 3627–33

[49] Qiu G *et al* 2004 Theoretical study of the surface energy and electronic structure of pyrite FeS_2(100) using a total-energy pseudopotential method, CASTEP *J. Colloid Interface Sci.* **270** 127–32

[50] Eggleston C M, Ehrhardt J J and Stumm W 1996 Surface structural controls on pyrite oxidation kinetics: an XPS-UPS, STM, and modeling study *Am. Mineral.* **81** 1036–56

[51] Rosso K M, Becker U and Hochella M F 1999 Atomically resolved electronic structure of pyrite (100) surfaces: An experimental and theoretical investigation with implications for reactivity *Am. Mineral.* **84** 1535–48

[52] Nair N N, Schreiner E and Marx D 2006 Glycine at the pyrite–water interface: the role of surface defects *J. Am. Chem. Soc.* **128** 13815–26

[53] Zhang Y N *et al* 2012 Effect of surface stoichiometry on the band gap of the pyrite FeS_2(100) surface *Phys. Rev.* B **85** 085314

[54] Bronold M, Tomm Y and Jaegermann W 1994 Surface-states on cubic d-band semiconductor pyrite (FeS_2) *Surf. Sci.* **314** L931–6

[55] Fiechter S *et al* 1992 The microstructure and stoichiometry of pyrite FeS_{2-x} *J. Mater. Res.* **7** 1829–38

[56] Yu L P *et al* 2011 Iron chalcogenide photovoltaic absorbers *Adv. Energy Mater.* **1** 748–53